INASTANTANEOUS BASELINE MULTIPLE DAMAGE DETECTION AND LOCALIZATION IN AN ALUMINUM PLATE USING LAMB WAVES

Behrouz Alem*, Ali Abedian*, Mostafa Nasiri*
* Aerospace engineering Department, Sharif University of Technology, Tehran, Iran

Mail: b_alem@ae.sharif.edu, phone+98-(0)21-661-4647

Abstract

In recent years, new Structural Health Monitoring (SHM) methodologies with a concept of "instantaneous baseline damage detection" are being developed by many researchers. In this context, this paper uses a new method to identify multiple damage in the aluminum plate. For this goal use from spars PZWS sensor network to generate and received guided waves. Ultrasonic waves are generated and measured from all possible different pairs of excitation and sensing transducers. For feature extraction of received signals used from continues wavelet transform. A probabilistic damage diagnostic algorithm based on correlation analysis was investigated to locate single or multiple damages. In this study, the method is validated using commercial finite element software to model the presence of 10 ultrasonic transducers bonded onto an aluminum plate.

1 Introduction

Lamb wave based active damage identification method is one of the most effective Structural Health Monitoring (SHM) techniques due to its excellent propagation capability even in materials with high attenuation and high sensitivity to local and small defects in plate-like structures. Several studies used the lamb waves-based damage diagnosis for simple geometry components such as large plates and could detect the notch cracks successfully [1-5].

Furthermore, some other studies have utilized the built-in piezoelectric transducers to monitor complex structural geometries (e.g. lap joints) [6, 7]. In majority of guided wave-based structural health monitoring (GW-SHM) algorithms, the damage is often identified by comparing the present signals captured from a potentially damaged condition of a structure with the baseline data captured from the pristine condition of the same structure (i.e. the structure without damage). The major concern with this methodology is the environmental and operational effects such as changes in temperature, surface moisture, and operational loads which can significantly affect the response signals and make it difficult to identify the structure defects [8-12]. To overcome this drawback, several researchers developed baseline free techniques which have no need of the baseline data [13-17]. Anton et. al. [18] proposed a baseline free method "instantaneous baseline measurements" based on the fact that lamb wave signals recorded for two equally spaced paths will be identical if no damage is present in the vicinity of the paths. Furthermore, a combination of probabilistic and imagining methods have been used in SHM. Correlation and probability-based damage identification methods were presented by several researchers. Wang et al. [19] combined the probabilistic methods and correlation analysis to detect the damage by means of guided wave propagation. Bagheri et.al [20] presented a reference-free approach for damage

identification and localization that combines the advantages of Continuous Wavelet Transform (CWT) and probabilistic methods with the need to deploy baseline-free systems. It is widely acknowledged that the identification of multiple damage using Lamb-wave-based algorithms can be highly uncertain or ambiguous, more specifically when assisted by an instantaneous method. In this study, we use a new instantaneous method to achieve more accurate identification of existence of multiple damages in a square aluminum plate.

The method is numerically validated by using finite element method and dynamic explicit time step analysis capability of ABAQUS, the existing standard commercial software.
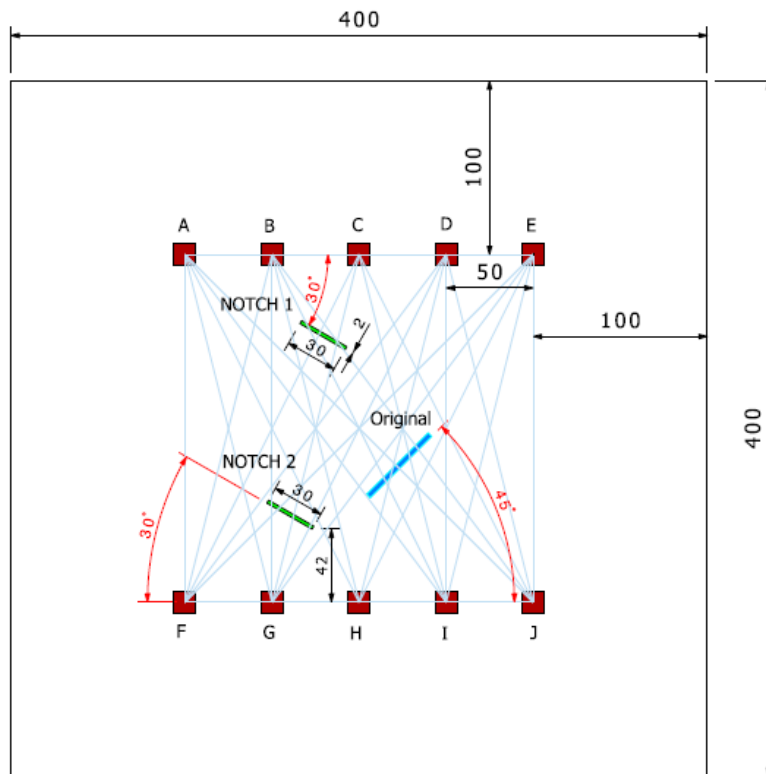

Fig. 1. Plate dimension and location of damages and of the sparse array (dimensions in mm)

2 Model description and the Numerical preparations

In this study, the sample model contains of ten (12.7mm by 12.7mm, 0.254 mm thick) embedded PZT transducers bonded to a square aluminum plate (400mm x 400mm x 5.08 mm thick) as shown in Fig. 1. Different damages were simulated in the form of a notch with dimensions described in table 1. Scenarios of existing damage illustrated in table 2.

Propagation of Lamb waves in a square aluminum plate was numerically simulated using the dynamic explicit time step analysis capability of ABAQUS 6.13, an existing standard commercial Software. The explicit solver provides a better trade-off between accuracy and the computational time. Several researchers have used the finite element method to simulate the propagation of lamb wave in metal and composite plate structures [21-25]. In dynamic time step analysis, stability and accuracy of the numerical solution depends greatly upon the temporal and the spatial resolution of the analysis. In most studies available in the literature, a minimum 20 points per cycle at the highest frequency (f_{max}) have been determined for time step (Δt) resolution. Usually, for spatial accuracy, element size (L) is

limited to one tenth of the wavelength (λ) of the A_0 (the anti-symmetric) mode, and at least two elements through the thickness of the plate, that is;

$$\Delta t < 1/(20 f_{max}), \; L_{min} \leq \lambda/10 \qquad (1)$$

It is notable that here convergence and mesh refinement studies showed that the anti-symmetric mode simulation requires a fine discretization through the sample thickness (more than 3 or 4 layers of elements through the thickness). But, in this study, only the symmetric portion of the received signals is used in signal processing and correlation analysis. Both piezoelectric transducer and aluminum plate were simulated by eight nodes standard solid elementsC3D8R with three degrees of freedom per node in ABAQUS element library. In this library there is also a multi-physics or fully coupled piezoelectric element which unfortunately can only be used in the time integration implicit solver. Therefore, in numerical modeling, the excitation wave in structure is applied to the nodes of transducer elements as nodal forces.

Table 1-Cut-through thickness damage dimensions

Damage	Dimension
Original notch 1	50 x 3 mm
Original notch 2	30 x 3 mm
Original notch 3	15 x 3 mm
Notch 1	30 x 2 mm
Notch 2	30 x 2 mm

Table 2-Scenarios of damage existence and combination.

Scenarios	Damage
1	Original notch 1
2	Original notch 2
3	Original notch 3
4	Notch 1
5	Notch 2
6	Original notch 1+ Notch 1
7	Original notch 1+ Notch 2

Modeling of piezoelectric sensor as tied to the structure makes it possible to achieve a more realistic simulation because the elastic effects of the piezo elements are considered. Lower surface of piezoelectric transducers was attached to the aluminum plate by 'tie' constraint in ABAQUS/Explicit and it has been arranged that the meshing pattern of the two connected regions to be the same. In tie constraint, the surface of actuator transducer is considered as the master region, while, the sensor surface is simulated as the slave region. The following properties were assumed for the homogenous, linear elastic, and isotropic material of the aluminum plate: ρ=2700kg/m^3, Young's modulus E=70.0 GPa, shear modulus G=25.94 GPa, and Poisson's ratio ν=0.33. Also, the homogeneous linear elastic and orthotropic properties were defined for piezoelectric transducers as follows; ρ=7700 kg/m^3, Young's modulus $E_1=E_2$ =70.0 GPa in plane and E_3=54.0 GPa in out of plane directions, shear modulus G=23.0 GPa, and Poisson's ratio ν=0.35.

Frequency of excitation signal which is entitled "tuning frequency" is an important parameter that must be correctly selected to achieve more accurate damage identification results. The frequency and number of cycles of the exciting signal are calculated according to the symmetric and anti-symmetric modes of output signals which are separated in pitch-catch method. This depends on the distance between actuator and sensor transducers and velocity of symmetric and anti-Symmetric waves or time flight of the waves. Therefore, a four-cycle sinusoidal tone burst electrical potential function having a 200-kHz center frequency and 10Vamplitude, peak to peak, was chosen for the actuator signal. Figs. 2(a) and (b) exhibit a Han-windowed excitation signal of 200 kHz in the time and frequency domains, respectively.

In numerical modeling, the excitation wave in structure is applied to the transducer nodes as nodal forces. Bagheri et al. [20] applied the excitation wave as out of plane nodal forces (normal to the surface) to the nodes of the structure corresponding to the middle point of the lower surface of the piezoelectric actuator attached to the plate. They claim this forcing function effectively excites the anti-symmetric

mode A_0 in the structure. However, in reality, the embedded piezoelectric transducer applies a mechanical strain to the structure in plane directions (not out of plain) because the upper surface of the actuator is in free condition. Furthermore, tuning the propagation of only symmetric or anti-symmetric waves in the structure can be influenced by some features such as, geometry of the PZTs, structure properties, and excitation wave frequency and this hypothesis does not depend on excitation direction. Though both symmetric and anti-symmetric modes of the response signals are informative in the lamb wave-based damage identification, only the symmetric portion of the receiving signals are used for damage detection purposes here in this study, which is more explained in the following section.
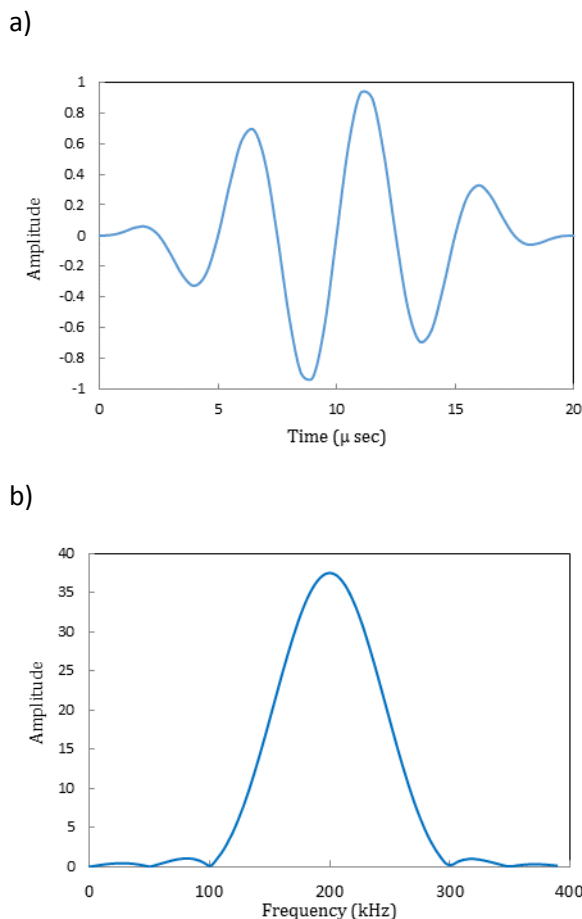
a)

b)

Fig. 2. (a) 4-cycle sine tone burst, (b) Fast Fourier transform of the 4-cycle tone burst.

Cho and Lissenden (2012) applied the load as concentrated force to the nodes around the perimeter of the transducer footprint, but the bending moments due to bending strain of the transducer element were neglected. However, in the present article, the elemental forces of each actuator, which induces the electrical strain in free condition to the structure, were calculated by the electromechanical coupling equation of piezoelectric materials. The constitutive equations describing the piezoelectric actuator behavior are based on the assumption that the total strain in the transducer is the sum of the mechanically induced strain due to the mechanical stress and the actuation strain caused by the applied electric voltage as follows [26]:

$$\varepsilon = S^E \sigma + d.E \qquad (2)$$

where, σ: stress vector, ε: strain vector, E: applied electric field vector, S^E: elastic compliance matrix and d: matrix of piezoelectric strain constants. The simulated square PZT patches of 12.7mm (0.5 in) length and 0.254 mm (0.01 in) thickness were selected from among the products of APC international, Ltd. The self-equilibrating nodal forces that the piezoelectric actuator exerts due to its working condition to the structure in directions 1 and 2 (Fig.3) are obtained by considering the mechanical normal stress applied on the lateral faces of simulating solid elements of each one of the actuators. Thus load induces the proportional strain to electrical strain due to electrical potential to the structure. It is oblivious that, the nodal loads on lateral faces of each element are determined by multiplying the normal stress to the related surface area which is then equally divided among the corresponding four nodes of each face of the element (Fig. 3). Reciprocally, the FEM strain or stress results of sensor elements can be used for calculation of the electric potential output of the sensor. The describing electromechanical equation for liner piezoelectric material can be presented as follows [26]:

$$D = \xi^\varepsilon E + e.\varepsilon \quad or \quad D = \xi^\sigma + d.\sigma \qquad (3)$$

Where D is the electrical displacement vector, **e** is the piezoelectric stress constant matrix, and ξ is the dielectric permittivity.
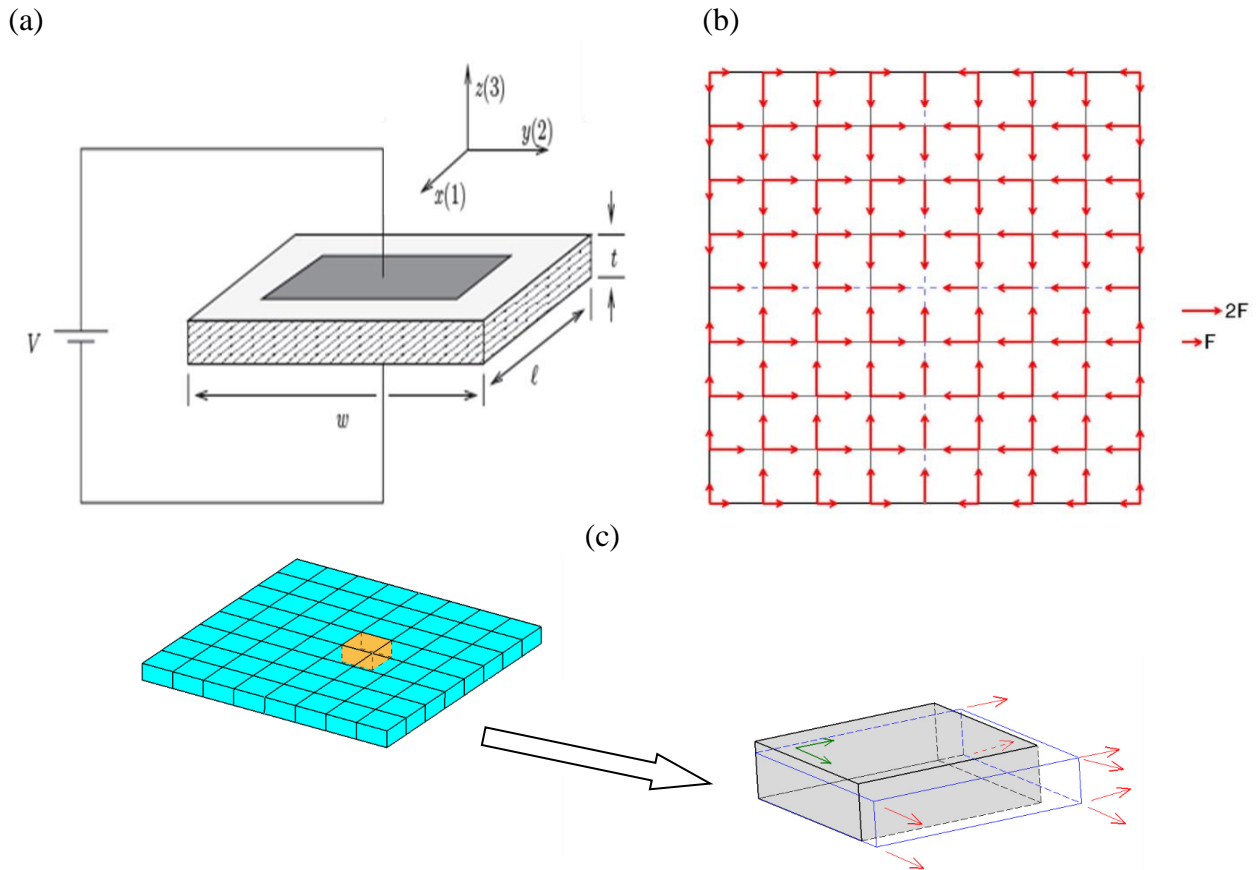
Fig. 3. Piezoelectric actuator elements and external loads. (a) Piezoelectric transducer schematic, (b) distribution of self-equilibrated nodal forces applied to actuator element nodes, (c) Transducer element and equivalent forces due to electrical strain.

3 Damage identification method

3.1 Continues Wavelet Transform

A simple instantaneous baseline free damage detection algorithm which was proposed by Anton and Inman [18], needs not any prerecorded data of the pristine structure. The main concept here is based on measuring the differences between the recorded signals along similar sensor-actuator paths, i. e. it relies on the fact that the recorded signals of two equal or similar paths should be identical if no defect is present in the vicinity of the paths. It is obvious that the transducers must be placed such that the paths are of equal length and that structural features are spatially uniform between transducers. When the lamb waves propagate through the structure incident to any

Discontinuity, transmission and reflection phenomena will be occurring and the comparison of differences in measured signals can be used to characterize the damages. In the present article, Continues Wavelet Transform (CWT), a powerful time-frequency analysis technique, is utilized for identifying the varying characteristics of dispersive guided wave signals [20, 27]. The CWT of a guided wave signal is a transformation that decomposes every such waves into a superposition of both scale and translation of a mother wavelet function $\psi(t)$ given by Eq. 4;

$$\psi_{a,\tau}(t) = |a|^{-\frac{1}{2}} \psi\left(\frac{t-\tau}{a}\right) \qquad (4)$$

Where the translation parameter τ shifts the wavelet in time, and the scaling parameter a controls the wavelet frequency band width. The CWT of a time-domain guided wave signal S(t) is defined as in Eq. 5;

$$W_\psi(a,\tau) = \frac{1}{\sqrt{a}} \int_{-\infty}^{\infty} S(t)\psi^*\left(\frac{t-\tau}{a}\right) dt \quad (5)$$

where ψ^* is the complex conjugate of ψ.

This algorithm uses the fact that the wavelet energy spectrum value of the recorded signal from the undamaged path is higher than that of any equal paths containing damages. This algorithm assumes that there is at least one healthy sensing path from the total of equal sensing paths. By the arrangement of transducers illustrated in Fig. 1, the number and the location of the transducers induced a total of 90 sensing paths resulting in 8 different path lengths. Table 3 clusters all the paths according to the actuator–sensor distance.

Table 3-The number of total paths and the geometric distances between each path.

Actuator-sensor distance (mm)	Sensing path	Total number of paths
50	AB, BC, CD, DE, FG, GH, HI, IJ (and vice versa)	16
100	AC, BD, CE, FH, GI, HJ (and vice versa)	12
150	AD,BE,FI,GJ (and vice versa)	8
200	AE, FG, AF, BG, CH, DI, EJ (and vice versa)	14
206	AG, BF, BH, CG, CI, DH, DJ, EI (and vice versa)	16
224	AH, BI, CF, CJ, DG, EH (and vice versa)	12
250	AI, BJ, DF, EG (and vice versa)	8
283	AJ, EF (and vice versa)	4

3.2 Feature extraction

From the waves' scalogram, the wavelet energy spectrum can be calculated as

$$E_j^i = |W_j^i(t,f)|^2, i = 1,2,\dots,n; \ j = 1,2,\dots,m(i) \quad (6)$$

where W_j^i is the scalogram associated with the jth guided wave signal associated with the ith sensing path. In the framework of the numerical analysis presented here n=8 and m =16 and 4 when i=1 and 8, respectively. From the scalogram, the following feature is computed

$$F_j^i = \sum_t \sum_f E_j^i(t,f) \ i = 1,2,\dots,n; \ j = 1,2,\dots,m(i) \quad (7)$$

where F is the CWT-based feature.

For each path distance, the maximum values F^i of the CWT based feature were calculated, and they identify the healthy condition of the structure.

3.3 Feature ratios and the probabilistic method

For each sensing path i, feature ratio (FR) were Defined as

$$FR_{i,j}^F = \left|\frac{F_j^i - F^i}{F^i}\right| \quad (8)$$

Then, the plate was meshed into a uniform 1x1mm grid. The probability P(x,y) that damage occurred at a grid node position (x,y) was defined as

$$p(x,y) = \sum_{i=1}^{n} \sum_{j=1}^{m} FR_{i,j} W_{i,j}[r_{i,j}(x,y)] \quad (9)$$

where $W_{i,j}[r_{i,j}(x,y)]$ is the probabilistic weight for the jth guided wave signal at the ith sensing path at (x, y), and $r_{i,j}(x,y)$ is the relative distance of the node (x, y) to the actuator and to the sensor associated with the jth guided wave signal at the ith sensing path, that is

$$r_{i,j}(x,y) = \frac{d_{i,j}^s + d_{i,j}^a}{d_{i,j}} - 1 \quad (10)$$

In equation (10), $d_{i,j}$ is the length of the actuator–sensor line of sight, $d_{i,j}^a$(x, y) is the node–actuator distance, and $d_{i,j}^s$ (x, y) is the node–sensor distance. The relative distance is zero at any grid node located along the line of sight of the actuator–sensor pair, and it linearly increases at locations away from that path. For illustrative purposes, the relative distance r of the sensing path AH is presented in Figure 5.
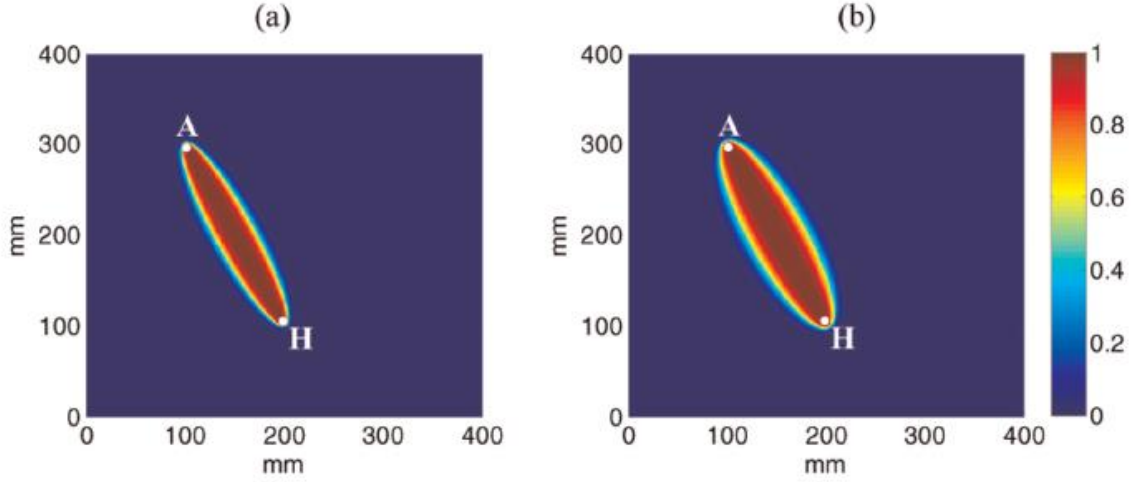
Fig. 4. Probabilistic weight W for the sensing path AH when (a) b = 0.02 and (b) b = 0.04 [20].
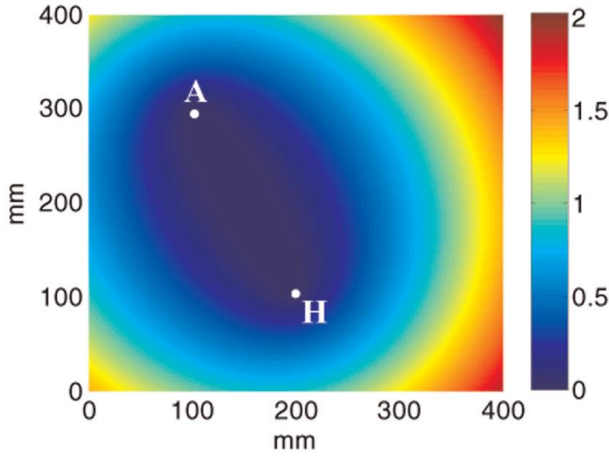

Fig. 5. Relative distance associated with sensing path AH [20].

In this study, the probabilistic weight was the Gaussian function:

$$W_{i,j}\left(r_{i,j}(x,y)\right) = exp\left[-\left(\frac{r_{i,j}(x,y)}{\beta}\right)^2\right] \qquad (11)$$

where β is a coefficient. The weight is a number comprised between 0 and 1. A weight equal to 1 indicates a point located on the line of sight between an actuator and a sensor, whereas a null weight is assigned to a point far from the sensing path. The constant β was determined by trial-and-error method, and it is dependent on the distance between transducers. A small coefficient reduces the zone of influence of the transducer pair. This means that flaws nearby the travel path across a pair of transducers might go undetected. Conversely, a large β expands the zone of influence of the probabilistic weight.

This, however, may cause unwanted overlap among different transducers' pairs of the array. Figure 4(a) and (b) shows the weight relative to path AH for $\beta = 0.02$ and $\beta = 0.04$. The difference in the ''area of influence'' between the two is evident. In this study, we used $\beta = 0.02$ as it proved a good trade-off between the sensitivity to damage and the broad coverage area. Finally, at each node (x, y) of the grid, the following discontinuity index (DI) was defined

$$DI(x,y) = \frac{p(x,y) - \mu_D}{\sigma_D} \qquad (12)$$

where μ_D and σ_D are the mean and standard deviation value of P(x,y), respectively. The index of equation (12) is normalized, and a threshold is applied such that all the values below the threshold are set to zero. In this study, we arbitrarily set the threshold to 0.8. It must be Emphasized that only the S0 mode propagating along the line of sight of each transducers' pair combination was considered in the analysis, and any contribution associated with the scattering, mode conversion, or reflections from the plate edges was ignored. This was done by gating the original window in order to include the first wave packet only in the analysis.

4 Damage detection results

Figure 6 shows the values of the 90 features F_j^i calculated according to equation (7).Each inset is relative to a specific actuator–sensor distance and refers to the results associated with the

propagation of the 4-cycle tone burst. For each inset, the values of the histograms are constant with the exception of those pairs that are affected by the presence of the original notch for scenario 1.
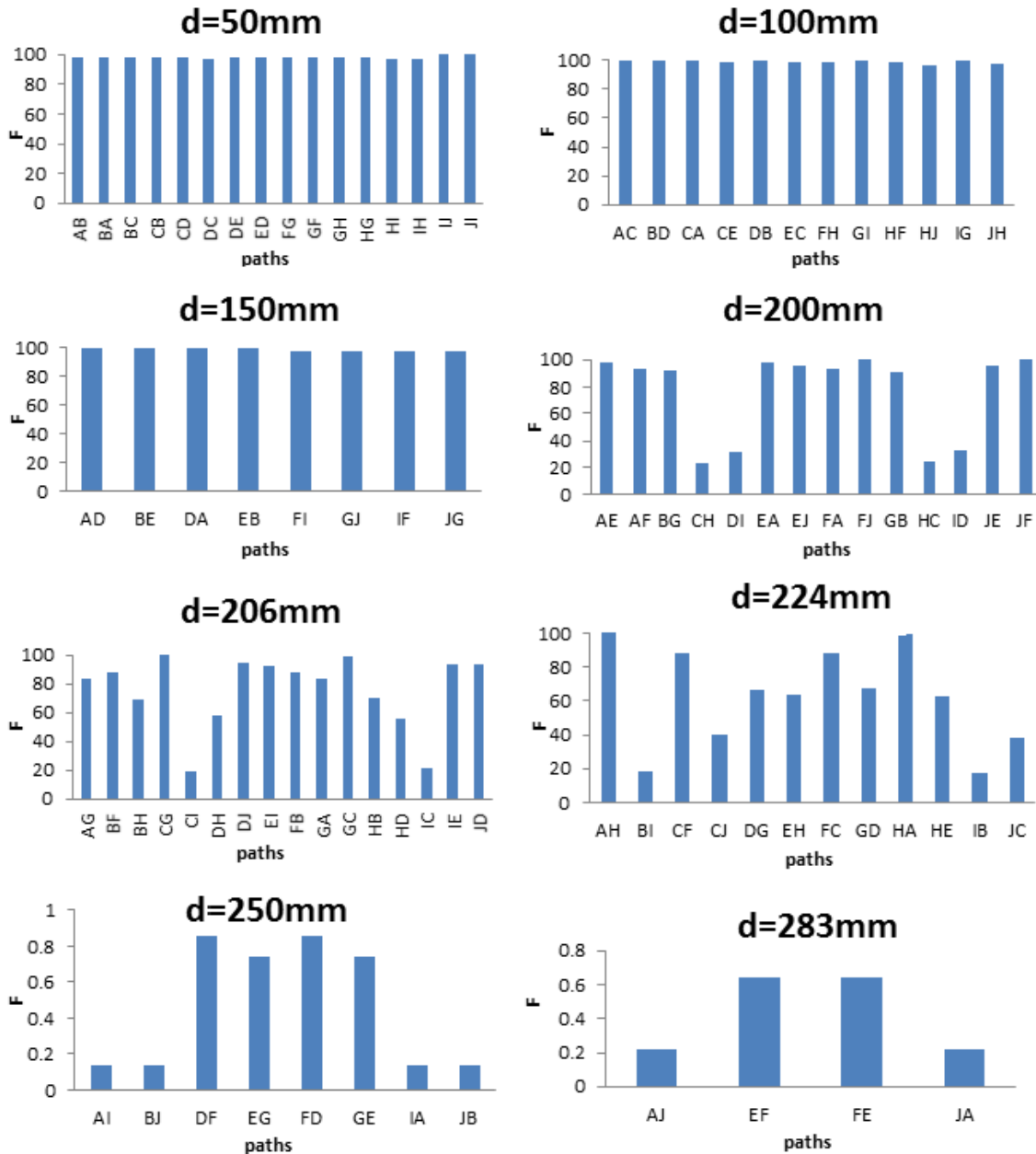

Fig. 6. Values of the CWT-based feature F for each sensing path for scenario 1. The results refer to the 4-cylce excitation source and are grouped according to the actuator–sensor distance (d).

By comparing the overall values of the CWT-based features, the histograms demonstrate that the damage is located along paths CH and DI (case with distance d = 200 mm), CI (d = 206 mm), BI and EH (d = 224 mm), AI and BJ (d =250 mm), and AJ (d = 283 mm). The results demonstrate that the approach is baseline free provided that part of the array is not affected by damage. In fact, the method does not consider any data taken from a pristine plate.

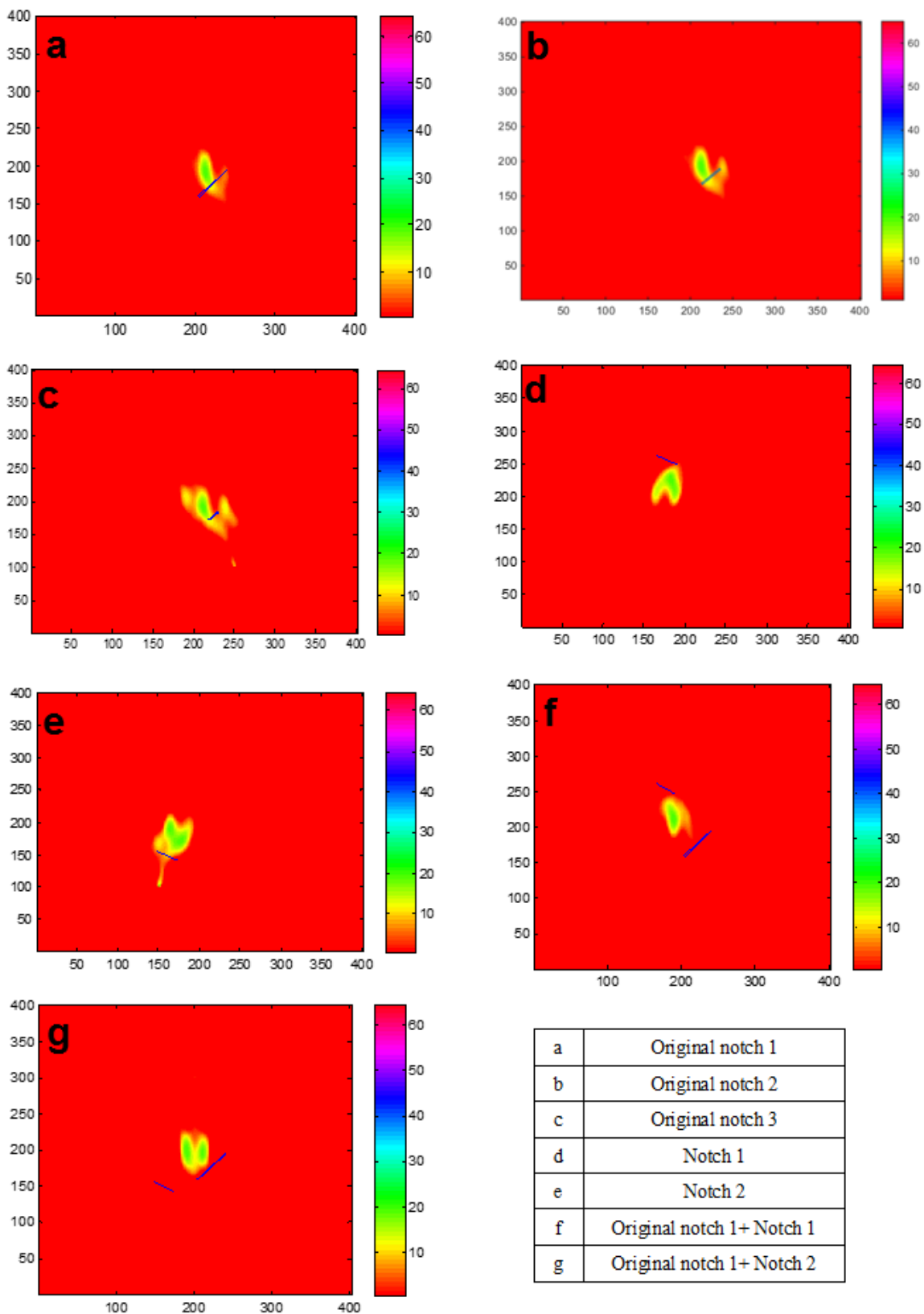| a	Original notch 1
b	Original notch 2
c	Original notch 3
d	Notch 1
e	Notch 2
f	Original notch 1+ Notch 1
g	Original notch 1+ Notch 2

Fig. 7. Mapping the discontinuity index on the plate using the CWT-based feature for 7 scenario.

Overall, the quantitative values of the feature are higher for the short distance cases. This is expected, as the wave beam attenuates due to the geometric expansion, and therefore, its energy per unit area diminishes. The results presented in Figure 6 indicate the presence of a structural anomaly but are unable to locate it precisely. The location of damage can be ascertained by applying the probabilistic method described in section ''Feature ratios and the probabilistic method''. Figure 7 shows the results of the localization algorithm when the CWT-based feature was applied to the 4-cycle excitation case. The contour plot describes the amplitude of the DI as computed by using equation (12) based on the CWT feature. The blue line overlapped to the image represents the position and the size of the notch. Owing to the threshold set in this study, the contour plot goes from 0.8 to 1, and all the DI below 0.8 were set to zero. The nonzero area is roughly orthogonal to the notch's direction because it is known that the effect of the notch on the wave amplitude is the largest when the direction of propagation is perpendicular rather than parallel to the damage Affected by the presence of the original notch for scenario 1. By comparing the overall values of the CWT-based features, the histograms demonstrate that the damage is located along paths CH and DI (case with distance d = 200 mm), CI (d = 206 mm), BI and EH (d = 224 mm), AI and BJ (d =250 mm), and AJ (d = 283 mm). The results demonstrate that the approach is baseline free provided that part of the array is not affected by damage. In fact, the method does not consider any data taken from a pristine plate. Overall, the quantitative values of the feature are higher for the short distance cases. This is expected, as the wave beam attenuates due to the geometric expansion, and therefore, its energy per unit area diminishes. The results presented in Figure 6 indicate the presence of a structural anomaly but are unable to locate it precisely. The location of damage can be ascertained by applying the probabilistic method described in section ''Feature ratios and the probabilistic method''. Figure 7 shows the results of the localization algorithm when the CWT-based feature was applied to the 4-cycle excitation case. The contour plot describes the

amplitude of the DI as computed by using equation (12) based on the CWT feature. The blue line overlapped to the image represents the position and the size of the notch. Owing to the threshold set in this study, the contour plot goes from 0.8 to 1, and all the DI below 0.8 were set to zero. The nonzero area is roughly orthogonal to the notch's direction because it is known that the effect of the notch on the wave amplitude is the largest when the direction of propagation is perpendicular rather than parallel to the damage.

5 Conclusion

In this paper, the wavelet transform was used to extract a robust and effective feature of received signals. This feature, called energy of signal from time domain, demonstrated a good resolution in a reference-free SHM approach to detect and localize existence of a single damage through the plate-like structure. This approach could not perfectly distinguish and localize the damages from together when there are two or more distinct damages through the structure. It was shown that there isn't good compatibility between the predicted and actual location of the damages defined in scenarios 4 and 5. This could be due to that a few number of sensing-paths are being dropped by the damages located in that positions. The future focus of this team will be about the improvement of the multi damage localization and optimization of sensor arrangement.

6 References

[1] Staszewski, W.J., B.C. Lee, and R. Traynor, *Fatigue crack detection in metallic structures with Lamb waves and 3D laser vibrometry.* Measurement Science and Technology, 2007. **18**(3): p. 727.

[2] Tua, P.S., S.T. Quek, and Q. Wang, *Detection of cracks in plates using piezo-actuated Lamb waves.* Smart Materials and Structures, 2004. **13**(4): p. 643.

[3] Giurgiutiu, V., A. Zagrai, and J. Bao, *Damage Identification in Aging Aircraft Structures with Piezoelectric Wafer Active Sensors.* Journal of Intelligent Material Systems and Structures, 2004. **15**(9-10): p. 673-687.

[4] Jagannathan, R., B. Krishnan, and C.V. Krishnamurthy, *A single transmitter multi-receiver (STMR) PZT array for guided ultrasonic wave based structural health monitoring of large isotropic plate structures.*

Smart Materials and Structures, 2006. **15**(5): p. 1190.

[5] Malinowski, P., et al., *A Phased Array-based Method for Damage Detection and Localization in Thin Plates.* Structural Health Monitoring, 2008.

[6] Ihn, J.-B. and F.-K. Chang, *Multicrack growth monitoring at riveted lap joints using piezoelectric patches.* 2002. **4702**: p. 29-40.

[7] Zhao, X., et al., *Active health monitoring of an aircraft wing with embedded piezoelectric sensor/actuator network: I. Defect detection, localization and growth monitoring.* Smart Materials and Structures, 2007. **16**(4): p. 1208.

[8] Sohn, H., *Effects of environmental and operational variability on structural health monitoring.* Philosophical Transactions of the Royal Society of London A: Mathematical, Physical and Engineering Sciences, 2007. **365**(1851): p. 539-560.

[9] Clarke, T., et al., *Evaluation of the damage detection capability of a sparse-array guided-wave SHM system applied to a complex structure under varying thermal conditions.* Ultrasonics, Ferroelectrics, and Frequency Control, IEEE Transactions on, 2009. **56**(12): p. 2666-2678.

[10] Marzani, A. and S. Salamone, *Numerical prediction and experimental verification of temperature effect on plate waves generated and received by piezoceramic sensors.* Mechanical Systems and Signal Processing, 2012. **30**: p. 204-217.

[11] Roy, S., et al., *A novel physics-based temperature compensation model for structural health monitoring using ultrasonic guided waves.* Structural Health Monitoring, 2014. **13**(3): p. 321-342.

[12] Wang, Y., et al., *An adaptive filter–based temperature compensation technique for structural health monitoring.* Journal of Intelligent Material Systems and Structures, 2014. **25**(17): p. 2187-2198.

[13] Park, H.W., et al., *Time reversal active sensing for health monitoring of a composite plate.* Journal of Sound and Vibration, 2007. **302**(1): p. 50-66.

[14] Sohn, H., et al., *Damage Detection in Composite Plates by Using an Enhanced Time Reversal Method.* Journal of Aerospace Engineering, 2007. **20**(3): p. 141-151.

[15] Gangadharan, R., et al., *Time reversal technique for health monitoring of metallic structure using Lamb waves.* Ultrasonics, 2009. **49**(8): p. 696-705.

[16] Agrahari, J.K. and S. Kapuria, *A refined Lamb wave time-reversal method with enhanced sensitivity for damage detection in isotropic plates.* Journal of Intelligent Material Systems and Structures, 2015.

[17] Seung Bum, K. and S. Hoon, *Instantaneous reference-free crack detection based on polarization characteristics of piezoelectric*

materials. Smart Materials and Structures, 2007. **16**(6): p. 2375.

[18] Anton, S.R., D.J. Inman, and G. Park, *Reference-free damage detection using instantaneous baseline measurements.* AIAA journal, 2009. **47**(8): p. 1952-1964.

[19] Dong, W., et al., *A damage diagnostic imaging algorithm based on the quantitative comparison of Lamb wave signals.* Smart Materials and Structures, 2010. **19**(6): p. 065008.

[20] Bagheri, A., K. Li, and P. Rizzo, *Reference-free damage detection by means of wavelet transform and empirical mode decomposition applied to Lamb waves.* Journal of Intelligent Material Systems and Structures, 2013. **24**(2): p. 194-208.

[21] Bartoli, I., et al., *Modeling guided wave propagation with application to the long-range defect detection in railroad tracks.* NDT & E International, 2005. **38**(5): p. 325-334.

[22] De Marchi, L., et al., *Prediction of pulse dispersion in tapered waveguides.* NDT & E International, 2010. **43**(3): p. 265-271.

[23] Moser, F., L.J. Jacobs, and J. Qu, *Modeling elastic wave propagation in waveguides with the finite element method.* Ndt & E International, 1999. **32**(4): p. 225-234.

[24] Sale, M., P. Rizzo, and A. Marzani, *Semi-analytical formulation for the guided waves-based reconstruction of elastic moduli.* Mechanical Systems and Signal Processing, 2011. **25**(6): p. 2241-2256.

[25] Cho, H. and C.J. Lissenden, *Structural health monitoring of fatigue crack growth in plate structures with ultrasonic guided waves.* Structural Health Monitoring, 2012. **11**(4): p. 393-404.

[26] *IEEE Standard on Piezoelectricity.* ANSI/IEEE Std 176-1987, 1988: p. 0_1.

[27] Niri, E.D. and S. Salamone, *A probabilistic framework for acoustic emission source localization in plate-like structures.* Smart Materials and Structures, 2012. **21**(3): p. 035009.

Copyright Statement